Japanese Journal of Applied Physics

REGULAR PAPER

Quantitative evaluation of implied open-circuit voltage after metal electrode deposition on TiO_x/Si heterostructures by photoluminescence imaging: impact of metallization on passivation performance

To cite this article: Shohei Fukaya *et al* 2023 *Jpn. J. Appl. Phys.* **62** SK1019

Japanese Journal of Applied Physics **62**, SK1019 (2023) **REGULAR PAPER**
https://doi.org/**10.35848/1347-4065/acc813**

Quantitative evaluation of implied open-circuit voltage after metal electrode deposition on TiO_x/Si heterostructures by photoluminescence imaging: impact of metallization on passivation performance

Shohei Fukaya[1*], Kazuhiro Gotoh[1], Takuya Matsui[2], Hitoshi Sai[2], Yasuyoshi Kurokawa[1], and Noritaka Usami[1*]

[1]*Department of Materials Process Engineering, Graduate School of Engineering, Nagoya University, Furo, Chikusa, Aichi, 464-8603, Japan*
[2]*National Institute of Advanced Industrial Science and Technology, 1-1-1 Umezono-cho, Tsukuba, Ibaraki 305-8560, Japan*

[*]E-mail: fukaya.shohei.u3@s.mail.nagoya-u.ac.jp; usa@material.nagoya-u.ac.jp

Received December 26, 2022; revised March 20, 2023; accepted March 28, 2023; published online April 21, 2023

The degradation of surface passivation performance by metallization is a challenge in realizing highly efficient crystalline Si solar cells that use novel carrier-selective contacts. Here, we report on a simple method to study the effect of metallization on passivation of titanium oxide (TiO_x)/Si heterostructures. We investigated the relationship between the implied open-circuit voltage (iV_{OC}) and the photoluminescence (PL) intensity imaging of solar cell precursors before metallization. Based on the relationship obtained, the change of the iV_{OC} before and after metallization on the TiO_x was evaluated quantitatively. The results showed that the iV_{OC} predicted by the PL measurement decreases by 23–104 mV after metal deposition and shows a good agreement with the measured V_{OC} in the finished solar cells. These results demonstrate that the iV_{OC} evaluation by PL measurement provides a good prediction of the V_{OC} after metallization, which is useful in analyzing the passivation degradation induced by metallization.

Supplementary material for this article is available online

1. Introduction

High-performance solar cells are essential, particularly for building- and vehicle-integrated photovoltaic applications. Silicon heterojunction (SHJ) solar cells using hydrogenated amorphous silicon (a-Si:H) as carrier-selective contacts (CSCs) have achieved a high power conversion efficiency (PCE) of >25%, which is enabled by the high passivation performance at the interface between crystalline Si (c-Si) and the intrinsic a-Si:H [a-Si:H(i)] layer, and by the excellent carrier selectivity of doped a-Si:H.[1–4)] However, the energy loss still remains due to parasitic absorption in the short wavelength region caused by its low bandgap energy (E_g) of 1.7 eV.[5,6)] In addition, the cost of a-Si:H film formation is still high, and therefore, it is necessary to design a new material that has a higher E_g and can be fabricated with a simple fabrication method for practical use.

To further improve the PCE of SHJ solar cells at a reduced cost, recent studies have focused on applying novel CSCs. CSCs are required to efficiently select and extract the carriers (electrons and holes) with high passivation performance. Replacing a-Si:H with a wider bandgap CSC material is attractive to reduce the parasitic absorption that was observed in the conventional SHJ solar cells. There are several candidates for CSCs: molybdenum oxide (MoO_x),[7–9)] vanadium oxide (V_2O_x),[10,11)] copper iodide (CuI),[12,13)] nickel oxide (NiO_x),[14)] magnesium oxide (MgO_x)[15–17)] and titanium oxide (TiO_x).[18–27)] Among them, TiO_x has been intensively studied as an electron-selective contact (ESC) which selectively collects electrons. In principle, TiO_x is much less prone to absorbing light than a-Si:H due to its wider E_g of 3.3 eV. Furthermore, TiO_x/c-Si heterostructure can efficiently collect electrons due to its small conduction band offset (<0.05 eV) and large VB offset (>2.0 eV).[28,29)] In addition, the atomic layer deposition (ALD) of TiO_x has an advantage that the amorphous TiO_x is uniformly deposited at the nanoscale and provides good passivation of the Si surface. Consequently, high PCE has been reported for solar cells using TiO_x.[18,25,27)] Note that TiO_x can also work as a hole-selective contact by modifying the growth and the post annealing processes.[27)] However, we focus on TiO_x as an ESC in this work.

Although TiO_x has these advantages, it has not yet been used in practical devices owing to some issues, for example, a high interface resistivity at the TiO_x/metal contact[30)] and degradation of passivation performance after metallization.[31)] To solve the former issue, the attempts that use low-work function materials are made to introduce downward band bending. In fact, there are some reports to lower the contact resistivity by inserting low-work function materials such as LiF,[32)] Ca,[33)] and Mg.[34)] On the other hand, the latter issue has not been addressed yet, and the degradation mechanism has not been fully understood. Therefore, mitigating the metallization-induced degradation is essential to use TiO_x as an ESC in practical Si solar cells.

To understand the degradation mechanism, a quantitative evaluation of the passivation performance after metallization is essential. In general, implied open-circuit voltage (iV_{OC}) is measured by the quasi-steady-state photoconductance (QSSPC) method and commonly used as an index of passivation performance. However, in principle, QSSPC is not applicable to metallized cell precursors because the conductance of metals is much higher than the photoconductance of Si wafers. Although open-circuit voltage (V_{OC}) can be measured with finished solar cells, it is extremely time- and resource-consuming. Therefore, a quick and contact-less technique that enables to quantify the iV_{OC} of metallized cell precursors is highly desired. Hallam et al. reported that iV_{OC} correlates with photoluminescence (PL) intensity (I_{PL}) if the samples have the same surface structure, and the I_{PL} is converted into iV_{OC} by using a calibration line.[35)] This non-destructive and contact-less approach is applicable to solar cells even after metallization and suited to characterize the iV_{OC} before and after metallization quickly.

In this study, we focused on the TiO_x/Si heterostructures fabricated for ESC and evaluated the iV_{OC} before and after metal deposition quantitatively by PL using a calibration line obtained from the relationship between pre-measured iV_{OC}

and I_{PL}. Then, we tested the validity of the results by comparing the predicted iV_{OC} based on PL with the V_{OC} of the finished solar cells.

2. Experimental methods

All experiments were performed on double side mirror-polished, n-type c-Si(100) wafers. The resistivity and thickness were 1.0–5.0 Ω·cm and about 280 μm, respectively. An intrinsic and p-type a-Si:H (p/i) layer was deposited by plasma-enhanced CVD (PECVD) on the front side. The growth conditions of the p-type a-Si:H (p/i) layers were reported elsewhere.[36] After that, the substrates were immersed in a 5% HF solution to remove the native oxide layer on the rear side. Then TiO_x was deposited on the rear side by thermal ALD (GEMStar-6, Arradiance Inc.). Tetrakis-dimethyl-amido-titanium (TDMAT), water vapor, and nitrogen (99.9999%) were used as a titanium precursor, oxidant, and purging gas, respectively. The TDMAT precursor bottle was heated at 60 °C during the ALD process. The titanium precursor supply line was maintained at 115 °C to avoid precursor condensation. The deposition temperature was 150 °C. The dose durations of TDMAT and H_2O were 700 and 22 ms, respectively. The purge durations for TDMAT and H_2O were 23 and 28 s, respectively. The TiO_x thickness was varied in the range of 1–6 nm. After the TiO_x deposition, hydrogen plasma treatment (HPT) was performed to improve the passivation performance.[37] There are many process parameters for HPT, including process temperature (T_{HPT}), process time (t_{HPT}), H_2 pressure (p_{H2}), H_2 flow rate (R_{H2}), RF power (P_{RF}), and electrode distance (d). In this study, these parameters were set at T_{HPT} = 373 K, t_{HPT} = 90 s, p_{H2} = 100 Pa, R_{H2} = 70 sccm, P_{RF} = 390 W, d = 10 mm based on our previous work.[37] After TiO_x deposition, Mg and Al layers were subsequently deposited on the TiO_x as electrodes by thermal evaporation. The Mg electrode was employed to reduce the contact resistance.[34] After each process, the iV_{OC} and I_{PL} (PL intensity per unit second) of the fabricated samples were measured by the QSSPC system (WCT-120TS, Sinton Instrument Inc.) and the PL imaging system (EPL-100s, Hamamatsu Photonics), respectively. After metal electrode deposition, only I_{PL} was measured. A schematic of sample structures for iV_{OC} and I_{PL} measurements is shown in Figs. 1(a) and 1(b). In this study, the iV_{OC} and I_{PL} represent the averaged values over the 4 cm square in the center of the sample. The wavelength and intensity of the excitation light for the PL imaging were 940 nm and 100 mW cm^{-2}, respectively. After the measurement of I_{PL}, an indium tin oxide (ITO) layer and silver grid electrodes on the p-type a-Si:H [a-Si:H(p)] layer were deposited by sputtering with shadow masks to obtain the finished solar cells, followed by annealing at 160 °C for 2 h. The area of the substrates was 25 cm^2, and the area of the finished solar cells defined by the front ITO layer was 1.12 cm^2. A schematic structure of the fabricated solar cell is depicted in Fig. 1(c-1). The actual layout of the fabricated solar cell structure is shown in Fig. 1(c-2). Current–voltage (I–V) measurements were carried out under one Sun (air mass 1.5 global, 100 mW cm^{-2}) illumination generated by a solar simulator to measure the V_{OC} of solar cells. A shading mask was used to define the illumination area (1.045 cm^2) slightly smaller than the cell area.

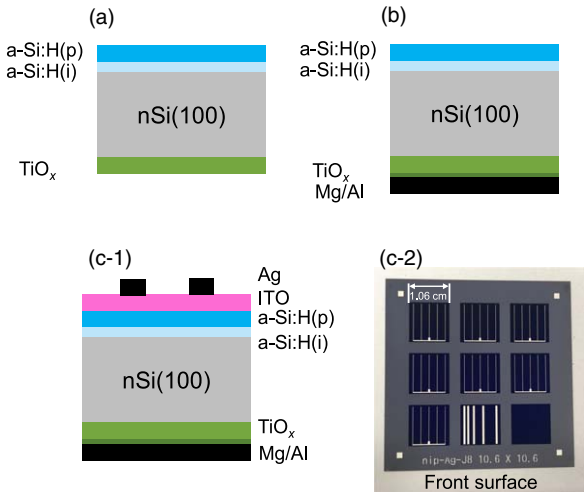

Fig. 1. Schematic sample structures for (a) iV_{OC} and I_{PL} measurements before metallization, (b) I_{PL} measurements after metallization, (c-1) V_{OC} measurements, and (c-2) a photograph of the solar cells (1.12 cm^2) fabricated on a 5 cm x 5 cm c-Si substrate.

3. Results and discussion

Figure 2 shows (a) the injection-level-dependent effective lifetime (τ_{eff}) and (b) the iV_{OC} before and after HPT for various TiO_x thicknesses. The iV_{OC} values of an p/i/N/TiO_x heterostructure before and after HPT with a 1 nm thick TiO_x are shown in Fig. 2(a). Note that p, i, N represent a-Si:H(p), a-Si:H(i), and n-type c-Si wafer, respectively. It should be noted that the τ_{eff} of the samples is predominantly limited by the passivation performance of the TiO_x side, which was confirmed by measuring the τ_{eff} of a symmetrically passivated sample (i.e. $\tau_{eff} \sim 4 \times 10^{-3}$ s was obtained in a p/i/N/i/p heterostructure at minority carrier density of 1×10^{15} cm^{-3}). From Fig. 2(a), it was found that when the TiO_x thickness was 1 nm, the sample showed a significant improvement in the passivation performance from an iV_{OC} of 649 to 692 mV by HPT. This is possibly because the dangling bonds at the TiO_x/c-Si interface were terminated by hydrogen. After HPT, however, the passivation performance was improved only for the sample with the TiO_x thickness of 1 nm whereas it was degraded significantly for larger thicknesses, as shown in Fig. 2(b). In our previous work, we have reported that the best passivation performance was observed for the 1 nm thick TiO_x/c-Si heterostructure after the HPT.[37] One possible cause of this degradation is due to the UV light soaking generated by HPT,[22] or the insufficient penetration of hydrogen radicals into the TiO_x/Si interface when the TiO_x film is thick. These results show that HPT under unsuitable conditions could cause considerable damage to the cell performance. However, the mechanism for the effect of HPT is still not well understood, and further investigations are necessary. Hereafter, we focus on our optimum TiO_x/Si heterostructure with a 1 nm thick TiO_x.

Figure 3 show the PL images of a p/i/N/TiO_x heterostructure (a) before and (b) after the deposition of the Mg/Al electrode on the TiO_x film (rear side). From the PL images, it is seen that the I_{PL} is reduced from 1×10^4 to 2×10^3 counts s^{-1} by the rear metal electrode deposition. Here we note that the I_{PL} of the metallized samples was corrected by subtracting the PL signal component arising from the

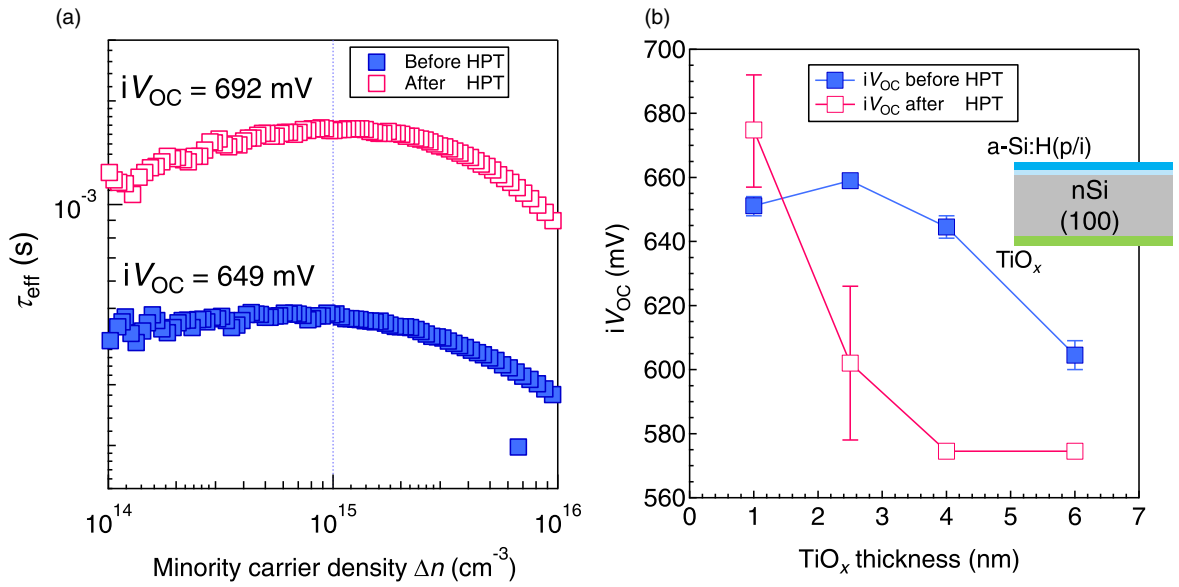

Fig. 2. (a) Injection-dependent τ_{eff} for a p/i/c-Si/TiO_x heterostructure with 1 nm thick TiO_x. (b) iV_{OC} before and after HPT as a function of TiO_x thickness. The inset shows a schematic of measured samples.

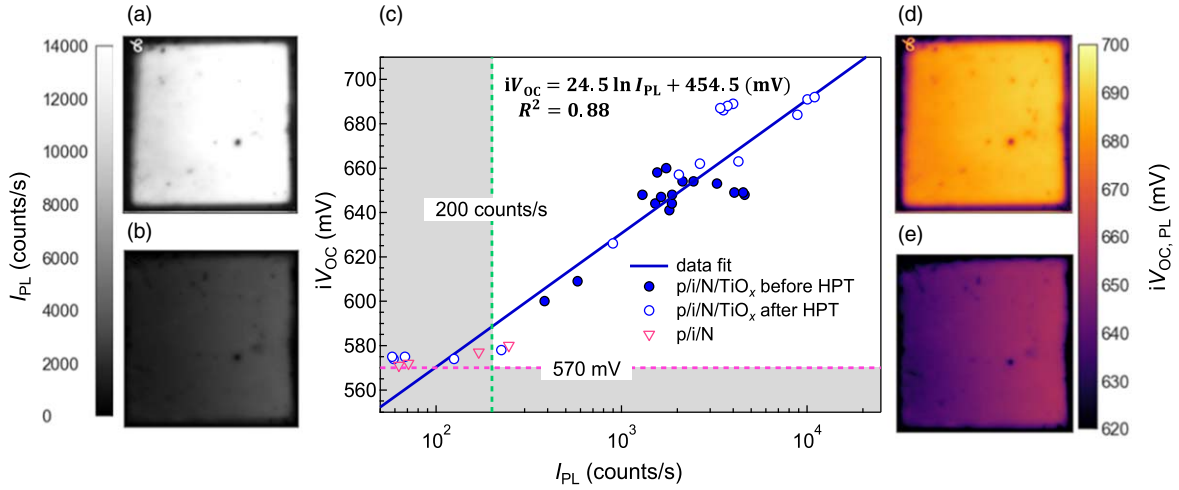

Fig. 3. PL images of the p/i/c-Si/TiO_x heterostructure (a) before and (b) after metallization. (c) Correlation between the iV_{OC} and I_{PL} of the heterostructures before depositing metal on TiO_x. The iV_{OC} images calculated from the calibration line and I_{PL} (d) before metallization, and (e) after metallization.

reflection at the metallized rear surface (supporting information, Fig. S1). Figure 3(c) shows the relationship between iV_{OC} and I_{PL} for each sample before metallization. The iV_{OC} and I_{PL} of the p/i/N heterostructures without any passivation layer at the rear side were measured to be 570 mV and 200 counts s^{-1}, respectively, which are considered as the lowest values of the poorly passivated sample. Thus, the samples showing $iV_{\mathrm{OC}} < 570$ mV and $I_{\mathrm{PL}} < 200$ counts s^{-1} were excluded from the linear regression to make an iV_{OC} - I_{PL} calibration line. From Fig. 3(c), a linear correlation was found between iV_{OC} and the logarithm of I_{PL}. The calibration line can be expressed as the following equation[35)]

$$iV_{\mathrm{oc}} = C_1 \cdot k_{\mathrm{B}}T\ln(I_{\mathrm{PL}}) + C_2 \quad (1)$$

where C_1 and C_2 are constant prefactors, k_{B} is the Boltzmann constant, and T is temperature. Here, the temperature was 295 K, which gives $k_{\mathrm{B}}T = 25.4$ mV. As shown in Fig. 3(c), the iV_{OC} is well correlated with I_{PL} with a coefficient of determination R^2 of 0.88 in the range from 574 to 692 mV, which is in good agreement with the previous report.[35)] The relatively large deviation seen for some samples is probably caused by the poor uniformity in the rear surface passivation, as the measured areas for the iV_{OC} (~3 cm^2) by QSSPC and for the I_{PL} (~16 cm^2) are different. Since the TiO_x thickness is as thin as 1 nm in this study, the TiO_x thickness nonuniformity even at a sub-nanometer scale is expected to cause a relatively large performance difference. Therefore, it is plausible that these anomalous values occur when the measurement areas of iV_{OC} and I_{PL} are not identical. Figures 3(d) and 3(e) show the $iV_{\mathrm{OC,PL}}$ images before and after metallization, respectively, which were calculated using the I_{PL} mapping and the calibration line. From $iV_{\mathrm{OC,PL}}$ images, the areal distributions of $iV_{\mathrm{OC,PL}}$ values can be visualized. The differences between the maximum and minimum $iV_{\mathrm{OC,PL}}$ values are 29 mV before metallization and 54 mV after metallization, respectively. The tendency of the larger areal distribution of the $iV_{\mathrm{OC,PL}}$ after metal electrode deposition was consistently observed in various samples, suggesting that the non-uniform metal formation on the TiO_x layer influences the passivation performance.

Figure 4 shows the map of the saturation current density J_0 (fA cm^{-2}) (a) before HPT, (b) after HPT, and (c) after metallization. These maps were obtained using the following equation:

$$V_{OC} = \frac{k_B T}{q} \ln\left(\frac{J_{SC}}{J_0} + 1\right) \quad (2)$$

Here, $iV_{OC,PL}$ is used instead of V_{OC}. q and J_{SC} represent the elementary charge and the short-circuit current density, respectively. The J_{SC} is assumed to be 32 mA cm^{-2} based on the actual values measured on the finished solar cells. As clearly seen in Fig. 4, we can confirm the decrease of J_0 after HPT and the increase of J_0 after metallization.

The actual V_{OC} of solar cells was measured after the front electrode (ITO and Ag finger) deposition [see Fig. 1(b)]. Figure 5(a) shows the comparison between iV_{OC} measured before metallization (open symbols) and V_{OC} after metallization (closed symbols) of solar cells plotted against their corresponding $iV_{OC,PL}$. The iV_{OC} data in Fig. 5(a) represents only before metallization. The difference in the number of open and closed symbols is due to our experimental process, in which the V_{OC} of several solar cells was measured from a substrate while the single iV_{OC} was measured from a substrate. From Fig. 5(a), iV_{OC} for the unmetallized sample and V_{OC} for the metallized sample agree relatively well with $iV_{OC,PL}$, respectively. A slight deviation of V_{OC} from $iV_{OC,PL}$ will be discussed later. However, a substantial gap is found between i*V*oc before metallization and *V*oc after metallization in all samples. This gap indicates that passivation degradation by metal deposition occurs. Figure 5(b) shows the box and swarm plots of the $iV_{OC,PL}$ difference before and after metallization ($\Delta iV_{OC,PL}$). The $\Delta iV_{OC,PL}$ is defined as the following equation,

$$\Delta iV_{OC,PL} = iV_{OC,PL} \text{ before metallization} - iV_{OC,PL} \text{ after metallization.} \quad (3)$$

From Fig. 5(b), metallization-induced passivation degradation, which is represented as $\Delta iV_{OC,PL}$, was found in the range of 23–104 mV. Although the $\Delta iV_{OC,PL}$ differs from batch to batch of the sample processes, the samples exhibiting high passivation performance result in a large $\Delta iV_{OC,PL}$ as a general trend. This indicates that the passivation quality of the solar cells using the TiO_x ESC is primarily limited by the metallization-induced passivation degradation.

From Fig. 5(a), it is found that V_{OC} of all solar cells are lowered compared to the $iV_{OC,PL}$. To discuss the reliability of the calibrated $iV_{OC,PL}$ with respect to the measured V_{OC} of the solar cells, the gap between the $iV_{OC,PL}$ and the V_{OC} of the finished solar cells (ΔV_{OC}) is plotted in Fig. 5(c). The ΔV_{OC} is expressed as

$$\Delta V_{OC} = iV_{OC,PL} - V_{OC}. \quad (4)$$

It is found that the ΔV_{OC} values are within the range of $-4 < \Delta V_{OC} < 38$ mV. This gap is possibly caused by the V_{OC} loss due to the imperfect carrier selectivity of both the TiO_x electron contact and the a-Si:H(p) hole contact, as well as the process-induced damage caused by the sputtering of the ITO and Ag electrodes, and the following post-deposition annealing. Another possible cause is the perimeter effect[38] where the photogenerated carriers diffuse out from the cell edge toward the unilluminated region and thus carrier density in c-Si is decreased. This effect is more pronounced in the case of small area solar cells with high quality Si absorbing layers. Note that the cell area is defined in 1 cm^2 using a shadow mask in this study. Further, high-quality Fz Si wafers were used as substrates. Hence, V_{OC} were expected to be reduced to some extent owing to the perimeter effect.

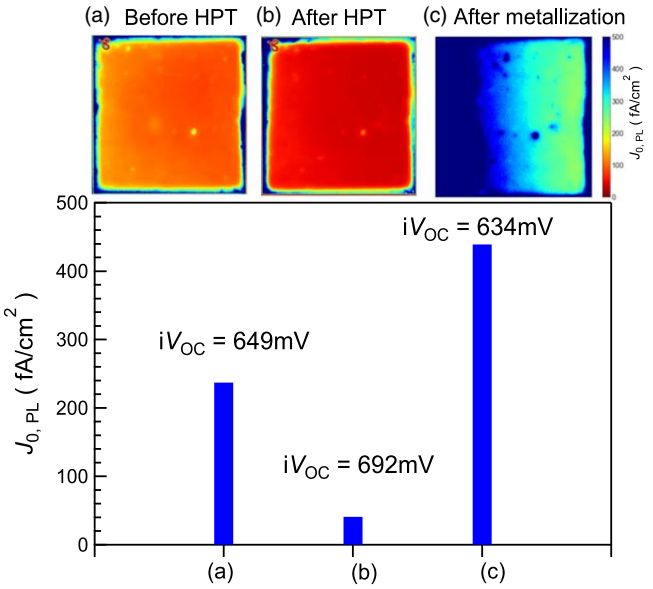

Fig. 4. Saturation current density J_0 calculated from $iV_{OC,PL}$ (a) before HPT, (b) after HPT, and (c) after metallization. The images represent $J_{0,PL}$ mappings.

Finally, we touch on the versatility of the method presented in this study. It is important to note that there exists an upper or lower performance limit for the PL imaging and QSSPC system if the passivation is too high or too low. In addition, since we have applied the method to our uncommon solar cell structures (i.e. a-Si:H(p)/a-Si:H(i)/c-Si/TiO_x/Mg/Al), further study is necessary to conclude whether or not this method can be applied to various types of Si solar cells. In principle, this method is also applicable to c-Si cells with textured surfaces as well, though we used only polished Si wafers within this work. In that case, however, the optical effects caused by surface textures must be taken into account, particularly for the rear side metallization. Nevertheless, the above results suggest that the method presented here can provide a quantitative measure of the V_{OC} loss caused by metallization and its post-fabrication processes of the solar cells that use novel CSCs.

4. Conclusions

The PL imaging technique was applied to quantitatively evaluate the iV_{OC} of metalized c-Si solar cell precursors, which was not measurable by common photoconductance methods such as QSSPC. We applied this method to evaluate the surface passivation quality of TiO_x-based CSCs in a-Si:H(p)/a-Si:H(i)/c-Si/TiO_x heterostructures, which was often deteriorated by the metallization process. By measuring iV_{OC} and I_{PL} for the samples exhibiting different degrees of surface passivation, we obtained a linear correlation between iV_{OC} and ln(I_{PL}), which was used to obtain $iV_{OC,PL}$. We confirmed a reduction in $iV_{OC,PL}$ of the Si heterostructures after the deposition of Mg/Al electrodes, indicating that the surface passivation at the TiO_x-based CSC was deteriorated

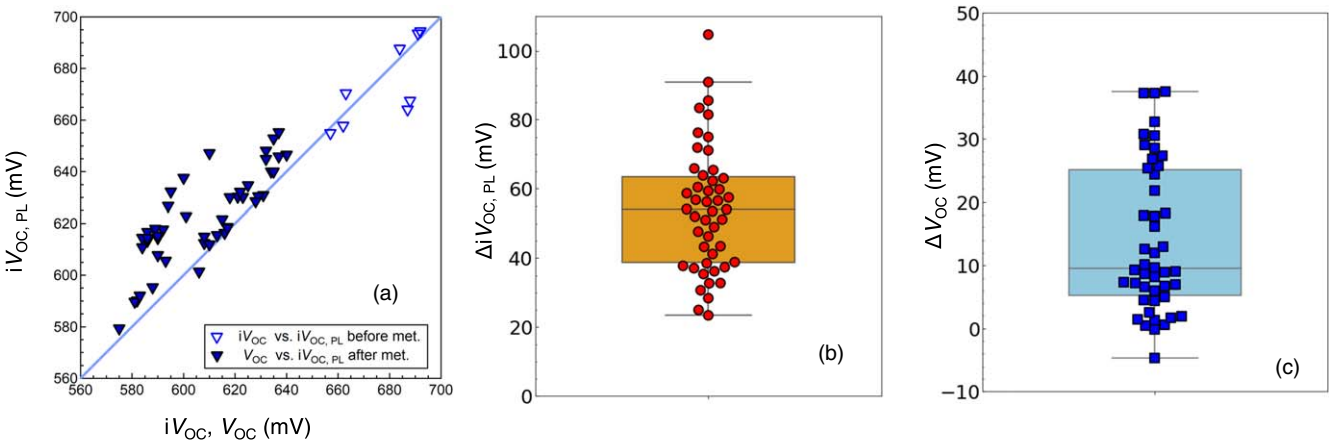

Fig. 5. (a) Plots of iV_{OC} and V_{OC} versus $iV_{OC,PL}$ for the samples above I_{PL} of 200 counts s^{-1} before and after metallization. (b) Box and swarm plots of $\Delta iV_{OC,PL}$ and (c) ΔV_{OC}.

by the metallization. A good agreement was observed between the $iV_{OC,PL}$ and the V_{OC} in the finished solar cells, suggesting that the PL imaging can be used to predict the V_{OC} of the finished solar cells and to analyze its loss caused by the metallization process. Thus, this method would help in the fast development of Si solar cells using novel metal-oxide based CSCs.

Acknowledgments

This work was supported by the New Energy and Industrial Technology Development Organization (NEDO), JPNP20005 and MEXT, Grants-in-Aid for Scientific Research on Innovative Areas "Hydrogenomics," JP18H05514 and JP18H05518.

ORCID iDs

Kazuhiro Gotoh https://orcid.org/0000-0002-4877-9370
Takuya Matsui https://orcid.org/0000-0003-1589-7052
Hitoshi Sai https://orcid.org/0000-0002-2938-551X
Yasuyoshi Kurokawa https://orcid.org/0000-0002-5319-3622
Noritaka Usami https://orcid.org/0000-0002-0602-2847

1) K. Yoshikawa et al., Nat. Energy **2**, 17032 (2017).
2) M. Taguchi, A. Yano, S. Tohoda, K. Matsuyama, Y. Yakamura, T. Nishiwaki, K. Fujita, and E. Maruyama, IEEE J. Photovolt. **4**, 96 (2014).
3) D. Adachi, J. L. Hernández, and K. Yamamoto, Appl. Phys. Lett. **107**, 233506 (2015).
4) K. Masuko et al., IEEE J. Photovolt. **4**, 1433 (2014).
5) Z. C. Holman, A. Descoeudres, L. Barraud, F. Z. Fernandez, J. P. Seif, S. D. Wolf, and C. Ballif, IEEE J. Photovolt. **2**, 7 (2012).
6) A. Langford, M. L. Fleet, and B. P. Nelson, Phys. Rev. B **45**, 13367 (1992).
7) J. Cho, N. Nawal, A. Hadipour, M. Recaman Payo, A. van der Heide, H. S. Radhakrishnan, M. Debucquoy, I. Gordon, J. Szlufcik, and J. Poortmans, Sol. Energy Mater. Sol. Cells **201**, 110074 (2019).
8) C. Battaglia, S. M. de Nicolás, S. de Wolf, X. Yin, M. Zheng, C. Ballif, and A. Javey, Appl. Phys. Lett. **104**, 113902 (2014).
9) J. Bullock, A. Cuevas, T. Allen, and C. Battaglia, Appl. Phys. Lett. **105**, 232109 (2014).
10) W. Wu, W. Lin, J. Bao, Z. Liu, B. Liu, K. Qiu, Y. Chen, and H. Shen, RSC Adv. **7**, 23851 (2017).
11) O. Almora, L. Gerling, C. Voz, R. Alcubilla, J. Puigdollers, and G. Garcia-Belmonte, Sol. Energy Mater. Sol. Cells **168**, 221 (2017).
12) K. Gotoh, M. Cui, I. Takahashi, Y. Kurokawa, and N. Usami, Energy Procedia **124**, 598 (2017).
13) H. Iimori, S. Yamane, T. Kitamura, K. Murakoshi, A. Imanishi, and Y. Nakato, J. Phys. Chem. C **112**, 11586 (2008).
14) F. Wang, H. Duan, X. Li, S. Yang, D. Han, L. Yang, L. Fan, H. Liu, J. Yang, and F. Rosei, Chem. Eng. J. **450**, 138060 (2022).
15) Y. Wan et al., Adv. Energy Mater. **7**, 1601863 (2017).
16) J. Yu, M. Liao, D. Yan, Y. Wan, H. Lin, Z. Wang, P. Gao, Y. Zeng, B. Yan, and J. Ye, Nano Energy **62**, 181 (2019).
17) H. Lin, D. Ding, Z. Wang, L. Zhang, F. Wu, J. Yu, P. Gao, J. Ye, and W. Shen, Nano Energy **50**, 777 (2018).
18) X. Yang, Q. Bi, H. Ali, K. Davis, W. V. Schoenfeld, and K. Weber, Adv. Mater. **28**, 5891 (2016).
19) T. Mochizuki, K. Gotoh, A. Ohta, S. Ogura, Y. Kurokawa, S. Miyazaki, K. Fukutani, and N. Usami, Appl. Phys. Express **11**, 102301 (2018).
20) K. Gotoh, T. Mochizuki, Y. Kurokawa, and N. Usami, Phys. Status Solidi A **216**, 1900495 (2019).
21) T. Mochizuki, K. Gotoh, Y. Kurokawa, T. Yamamoto, and N. Usami, Adv. Mater. Interfaces **6**, 1801645 (2019).
22) K. A. Nagamatsu, S. Avasthi, G. Sahasrabudhe, G. Man, J. Jhaveri, A. H. Berg, J. Schwartz, A. Kahn, S. Wagner, and J. C. Strum, Appl. Phys. Lett. **106**, 123906 (2015).
23) K. Gotoh, H. Miura, A. Shimizu, Y. Kurokawa, and N. Usami, Jpn. J. Appl. Phys. **60**, SBBF04 (2021).
24) K. Gotoh, T. Mochizuki, T. Hojo, Y. Shibayama, Y. Kurokawa, E. Akiyama, and N. Usami, Curr. Appl. Phys. **21**, 36 (2021).
25) J. Cho, J. Melskens, M. R. Payo, M. Debucquoy, H. S. Radhakrishnan, I. Gordon, J. Szlufcik, W. M. M. Kessels, and J. Poortmans, ACS Appl. Energy Mater. **2**, 1393 (2019).
26) T.-C. Chen, T.-C. Yang, H.-E. Cheng, I.-S. Yu, and Z.-P. Yang, Appl. Surf. Sci. **451**, 121 (2018).
27) T. Matsui, M. Bivour, M. Hermle, and H. Sai, ACS Appl. Mater. Interfaces **12**, 49777 (2020).
28) X. Yang, P. Zheng, Q. Bi, and K. Weber, Sol. Energy Mater. Sol. Cells **150**, 32 (2016).
29) S. Avasthi, W. E. McClain, G. Man, A. Kahn, J. Schwartz, and J. C. Sturm, Appl. Phys. Lett. **102**, 203901 (2013).
30) V. Titova, B. Veith-Wolf, D. Startsev, and J. Schmidt, Energy Procedia **124**, 441 (2017).
31) V. Titova and J. Schmidt, Phys. Status Solidi RRL **15**, 1 (2021).
32) W. Wang, J. He, D. Yang, C. Samundsett, S. P. Phang, Z. Huang, W. Shen, J. Bullock, and Y. Wan, Sol. Energy Mater. Sol. Cells **206**, 110291 (2020).
33) T. G. Allen, J. Bullock, Q. Jeangros, C. Samundsett, Y. Wan, J. Cui, A. Hessler-Wyser, S. De Wolf, A. Javey, and A. Cuevas, Adv. Energy Mater. **7**, 160260 (2017).
34) Y. Nakagawa, K. Gotoh, T. Inoue, Y. Kurokawa, and N. Usami, Phys. Status Solidi A **218**, 2100296 (2021).
35) B. Hallam, Y. Augarten, B. Tjahjono, T. Trupke, and S. Wenham, J. Appl. Phys. **115**, 239901 (2014).
36) H. Sai, H. Umishio, and T. Matsui, Sol. RRL **5**, 2100634 (2021).
37) S. Miyagawa, K. Gotoh, K. Kutsukake, Y. Kurokawa, and N. Usami, Sol. Energy Mater. Sol. Cells **230**, 111251 (2021).
38) F. Haase, S. Schäfer, C. Klamt, F. Kiefer, J. Krügener, R. Brendel, and R. Peibst, IEEE J. Photovolt. **8**, 23 (2018).

